PAPER

Facile synthesis of C–FeF₂ nanocomposites from CFx: influence of carbon precursor on reversible lithium storage†

M. Anji Reddy, [ID] *[a] Ben Breitung, [ID] [b] Venkata Sai Kiran Chakravadhanula, [ID] ‡[ab]
M. Helen,[a] Ralf Witte,[b] Carine Rongeat,[a] Christian Kübel, [ID] [abc] Horst Hahn[b]
and Maximilian Fichtner[ab]

Transition metal fluorides are an important class of cathode materials for lithium batteries owing to their high specific energy and safety. However, metal fluorides are electrical insulators, exhibiting slow reaction kinetics with Li. Consequently, metal fluorides can show poor electrochemical performance. Instead, carbon–metal fluoride nanocomposites (CMNFCs) were suggested to enhance electrochemical activity. Chemical synthesis of CMNFCs poses particular challenges due to the poor chemical stability of metal fluorides. Recently, we reported a facile one-step method to synthesize carbon–FeF₂ nanocomposites by reacting fluorinated carbon (CFx) with iron pentacarbonyl (Fe(CO)₅) at 250 °C. The method resulted in C–FeF₂ nanocomposites with improved electrochemical properties. Here, we have synthesized four different C–FeF₂ nanocomposites by reacting four different CFx precursors made of petro-coke, carbon black, graphite, and carbon-fibers with Fe(CO)₅. Electrochemical performance of all four C–FeF₂ nanocomposites was evaluated at 25 °C and 40 °C. It is shown that the nature of CFx has a critical impact on the electrochemical performance of the corresponding C–FeF₂ nanocomposites. The C–FeF₂ nanocomposites were characterized by using various experimental techniques such as X-ray diffraction, scanning electron microscopy, transmission electron microscopy, resistivity measurement, and ⁵⁷Fe Mössbauer spectroscopy to shed light on the differences in electrochemical behaviour of different C–FeF₂ nanocomposites.

Introduction

Conversion electrode materials based on metal fluorides are interesting as cathode materials for lithium batteries due to their high energy density compared to the insertion based electrode materials.[1–6] Metal fluorides react with lithium at a relatively high voltage, and more than one electron per metal can be transferred, which results in high energy density. For example, FeF₂ can react with 2.0 Li at a potential of 2.66 V, with a specific capacity of 571 mA h g⁻¹, which leads to a theoretical specific energy of 1518 W h kg⁻¹. On the other hand, metal fluorides pose certain challenges as electrode materials. Metal fluorides are electrical insulators, show slow reaction kinetics

with lithium, and consequently, they exhibit large voltage hysteresis between discharge and charge processes. In addition, high volume changes associated with metal fluorides pose further challenges.[4] Therefore, stable anchoring of metal fluoride nanocrystallites in a conductive carbon matrix is necessary to provide the electronic path, to improve the reaction kinetics and to buffer the volume changes. To overcome these issues, carbon metal fluoride nanocomposites (CMFNCs) were suggested in earlier work.[7,8]

A general approach to synthesize CMFNCs is mechanical milling of a conductive carbon with a desired metal fluoride.[7,8] While mechanical milling effectively reduces the particle size of metal fluorides, the high energy applied in mechanical milling process leads to the destruction of the original carbon structure and produces disordered carbons with less conductive interfaces. Consequently, CMNFCs obtained by mechanical milling show limited cycling stability in lithium half cells.[7,8] Alternatively, chemical methods have been reported to synthesize CMNFCs, which showed much higher cycling stability.[9–24] Recently, we have reported a facile method for the synthesis of carbon–metal fluoride nanocomposites by reacting graphite fluoride (CFx) with iron pentacarbonyl (Fe(CO)₅) at 250 °C.[25–27] The C–FeF₂ nanocomposites obtained by this method delivered

[a]Helmholtz Institute Ulm (HIU), Electrochemical Energy Storage, Helmholtzstr. 11, D-89081 Ulm, Germany. E-mail: munnangi.reddy@kit.edu

[b]Karlsruhe Institute of Technology (KIT), Institute of Nanotechnology (INT), Hermann-von-Helmholtz-Platz 1, 76344, Eggenstein-Leopoldshafen, Germany

[c]Karlsruhe Nano Micro Facility (KNMF), Karlsruhe Institute of Technology (KIT), Hermann-von-Helmholtz Platz 1, D-76344 Eggenstein-Leopoldshafen, Germany

‡ Presently at Materials Characterisation Division, Vikram Sarabhai Space Centre, Trivandrum, India.

high reversible capacity in lithium half cells.[25,27] Further, pretreatment of the CFx precursor by mechanical milling has a significant impact on the reversible capacity, which we attributed to the reduced particle size of CFx.[25] We also showed that optimum fluorine to carbon ratio is necessary to achieve high reversibility.[26]

CFx has a great advantage as a precursor material for the synthesis of CMFNCs, as it is a source of both conductive carbon and fluoride ions. Defluorination of CFx restores the carbon to its original state and the desired carbon structure can be pre-designed. More importantly, the reaction occurs in one step and is quick (could be finished in 1 h).[27] Further, addition of conductive carbon is not required to prepare the electrodes. In this study, we used various fluorinated carbon compounds namely, petro-coke, carbon black, graphite, and carbon-fibers to synthesize $C–FeF_2$ nanocomposites. The unique feature of such nanocomposites is that, while the average size of the FeF_2 crystallites is almost the same, the carbon matrix in which FeF_2 nanocrystallites are embedded is different. This provides a unique opportunity to study and better understand the requirements for the design of carbon-nanocomposites for high reversible lithium storage.

Experimental section

Synthesis

Different CFx precursors were kindly provided by Advanced Research Chemicals (ARC). $Fe(CO)_5$ was purchased from Aldrich. $C–FeF_2$ nanocomposites were synthesized in sealed Swagelok® type stainless steel (SS) reactors. In a typical synthesis, required amount of $Fe(CO)_5$ was added to 0.25 g of CFx powder in the SS reactor and closed with VCR fittings inside an argon-filled glove box. The SS reactor was placed inside a tube furnace, and the temperature was raised from room temperature to 250 °C with a heating rate of 5 °C min⁻¹. The reaction was carried out at 250 °C for 24 hours; then the reactor was allowed to cool down naturally. Pressure developed due to the formation of gaseous side product was released carefully, and the reactor was opened in the Ar-filled glove box. The resulting black powder was collected carefully.

Characterization

Powder X-ray diffraction (PXRD) patterns were recorded in Bragg–Brentano geometry in the 2θ range 10–70° using a Philips X'pert diffractometer equipped with Mo Kα radiation. In the Debye–Scherrer mode, patterns were collected using a STOE Stadi P diffractometer equipped with a Dectris Mython 1K linear silicon strip detector and Ge(111) double crystal mono-chromator (Mo Kα1 radiation, $\lambda = 0.7093$ Å). The samples were loaded into 0.7 mm glass capillaries (Hilgenberg borosilicate glass no 50) in an argon-filled glove box. For the refinement of the XRD pattern, we used MAUD software.[28] Scanning electron microscopy (SEM) was performed with a LEO 1530 at 15 kV using carbon tape as substrate. Transmission electron microscopy was carried out on an aberration (image) corrected Titan 80-300 (FEI Company) operated at 80 kV equipped with a Gatan

imaging filter Tridiem 863. The material for TEM studies consisted of powder sample free from solvents. Since the samples were sensitive to the electron beam at 300 kV, resulting in the amorphization of the graphitic carbon around the FeF_2 nanoparticles, the TEM studies were carried out at 80 kV. The Mössbauer spectra were collected using a standard transmission Mössbauer setup with a ^{57}Co in Rh-Matrix source operated in constant acceleration mode. All Isomer shifts (IS) are given with respect to bcc-Fe at room temperature. The spectra were fitted using the WinNormos software by R. A. Brand. For electrical resistivity measurements, the powders were pressed into a 13 mm diameter pellets with a pressure of 10 tons per m². The resistivity of the nanocomposites was measured by the Van der Pauw method.

Electrochemical studies

Electrochemical measurements were performed in Swagelok® type cells. The electrode fabrication and electrochemical cells were assembled in an argon-filled glove box. Electrodes were fabricated by mixing the as-synthesized material and poly-vinylidene fluoride (PVDF) in the weight ratios of 90 : 10. A slurry containing the above mixture was prepared by using *N*-methyl-2-pyrrolidinone and was spread on stainless steel (SS) foil (area: 1.13 cm²) and dried on the hot plate at 160 °C for 12 h. Typically, each electrode contained 4–6 mg of the $C–FeF_2$ nanocomposite. Lithium foil (Goodfellow) was used as the negative electrode, and a borosilicate glass fiber sheet (separator) saturated with 1 M $LiPF_6$ in 1 : 1 ethylene carbonate (EC)/dimethyl carbonate (DMC) (LP30, Merck) was used as the electrolyte. The cells were placed in an incubator (Binder) to maintain a constant temperature of 25 °C or 40 °C. Electrochemical studies were carried out using an Arbin battery cycling unit. For electrochemical impedance measurements (EIS), cells were assembled and equilibrated at open circuit voltage (OCV) for 24 h. Impedance measurements were made using Zahner IM6 electrochemical workstation.

Results and discussion

We used four different CFx precursors synthesized by fluorinating petro-coke (FPC), carbon-black (FCB), graphite (FG), and carbon-fibers (FCF) (Advanced Research Chemicals). These CFx precursors largely differ in terms of morphology, particle size and surface area (Source: Advanced Research Chemicals). Selected physical properties of these materials are given in Table S1 (see ESI†). In the case of FPC, FCB and FCF fluorine to carbon ratio is between 1.05–1.12, whereas in the case of FG it is 0.95. Fig. S1† shows the XRD patterns of the CFx precursors (see ESI†). All samples show two broad peaks: one at 5° and another at 18° which are typical for highly fluorinated carbon materials. Fig. S2† shows SEM images of the CFx precursors (see ESI†). In the case of FPC, the particle size is in the range of 1–30 μm, with an average particle size of 8.0 μm. In the case of FCB big agglomerates can be seen. However, these agglomerates consist of smaller particles which are less than 200 nm in diameter. In the case of FG, the particle size is in the range of 1–10 μm with

an average particle size of 2.0 μm. In the case of FCF, the diameter of the fibers is in the range of 10–30 μm while the length of the fibers is up to 100 μm. Despite the bigger particle size of the FCF, the surface area of 344 m² g⁻¹ suggests that the material is porous. The high surface area of the highly fluorinated carbons FCB (1.12) and FCF (1.1) suggests that during high-temperature fluorination some carbon was converted into a CF_4 gas which leads to pores.

Four types of C–FeF_2 nanocomposites were synthesized by reacting different CFx samples with $Fe(CO)_5$. PC–FeF_2 was synthesized by reacting fluorinated petro coke, FPC with $Fe(CO)_5$ for 24 h at 250 °C. Similarly, CB–FeF_2, G–FeF_2, and CF–FeF_2 were synthesized by reacting $Fe(CO)_5$ with FCB, FG, and FCF respectively at 250 °C for 24 h. Fig. 1 shows the XRD patterns of the as-synthesized carbon–FeF_2 nanocomposites recorded in capillary mode. In the case of PC–FeF_2, CB–FeF_2 and G–FeF_2 all the peaks could be indexed to rutile-type FeF_2. However, few extra peaks were observed in the case of CF–FeF_2 (indicated with an asterisk * in Fig. 1). We also noticed that the relative intensity of (210) plane is growing from CB–FeF_2 < PC–FeF_2 < G–FeF_2 < CF–FeF_2. The origin of the additional peaks could be due to the formation of iron carbide (which was confirmed by ⁵⁷Fe Mössbauer spectroscopy). Rietveld refinement was performed including iron carbide as a secondary phase. The carbon was not taken into account. The refinement parameters are given in Table S2 (see ESI†). The hump around 10° is due to the capillary and was fitted in the background using a Gaussian peak in addition to a polynomial function for the baseline. Further, refinement results showed that in the case of CB–FeF_2 there was no iron carbide whereas, in the case of PC–FeF_2, G–FeF_2 and CF–FeF_2 iron carbide was present as a secondary phase with a maximum of 22.5 wt% in CF–FeF_2. The average crystallite size was growing from PC–FeF_2 (11 nm) < G–FeF_2 (12 nm) < CF–FeF_2 (16 nm) < CB–FeF_2 (17 nm).

In order to further elucidate the origin of the additional reflections found in the XRD patterns, we recorded ⁵⁷Fe Mössbauer spectra of all the nanocomposites as Mössbauer spectroscopy is a sensitive local probe for the ⁵⁷Fe
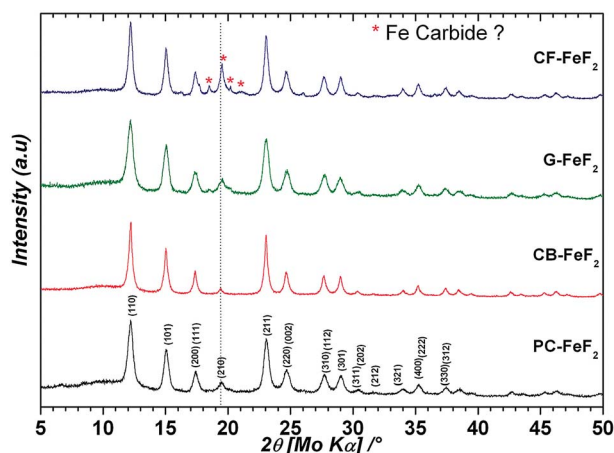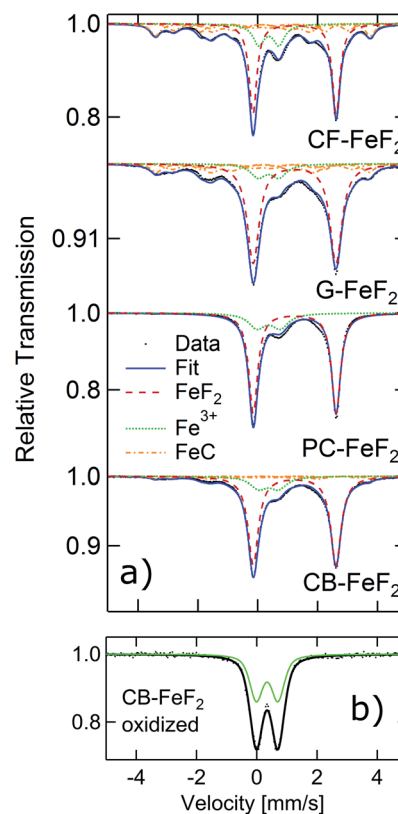

Fig. 2 Mössbauer spectra of C–FeF_2 nanocomposites measured at room temperature.

environments. Fig. 2a shows the measured Mössbauer spectra of the four C–FeF_2 nanocomposites together with their respective fit model. The obtained Mössbauer hyperfine parameters are summarized in Table S3 (see ESI†). All four samples show two quadrupole doublets as major components. The first one, and most important one is characteristic for FeF_2 with an IS of 1.33 mm s⁻¹, and a quadrupole splitting (QS) of about 2.77 mm s⁻¹. These values are in agreement with data in the literature.[29] The second doublet has an IS of about 0.47 mm s⁻¹, which is characteristic for the presence of Fe^{3+} component. However, no evidence was found for the existence of any crystalline phases of FeF_3 from the XRD measurements. This signal could be possibly due to aerial oxidation of the sample during the sample transfer, although care has been taken to avoid oxidation. This hypothesis has been checked by investigating a purposely air exposed sample (CB–FeF_2) (Fig. 2b). After exposure to air, the sample consists of pure Fe^{3+} components, which is very similar to the Fe^{3+} components found in the fresh samples. This finding makes the oxidation as an explanation for the occurrence of the Fe^{3+} phase very likely. The Mössbauer spectrum of the CB–FeF_2 sample was fully reproduced by these two doublets. All other samples exhibit three additional sub-spectra, which are magnetically split with a magnetic hyperfine field BHF of about 22, ~19 and ~11 T respectively. They can be attributed to the three Fe-sites present in $Fe_{1-x}C_x$ alloys ($x \sim 0.2–0.3$) with triangular, prismatic structure.[30] The relative ratios given in Table S3† describe the spectral area fraction of the sub-spectra

Fig. 1 XRD patterns of carbon–FeF_2 nanocomposites synthesized from various CFx precursors (recorded in capillary mode).

and may be used to compare the four samples among each other. However, it is not possible to give numbers for the phase fractions of the components as the Debye–Waller factors for these different phases may differ, which in turn leads to a different resonant area of the respective Fe environment.

From the XRD and Mössbauer studies, the presence of iron carbide is evident. Formation of iron carbide indirectly suggests the intermediate formation of iron nanoparticles by the decomposition of $Fe(CO)_5$; these iron nanoparticles further react with CFx and forms $C–FeF_2$. The absence of iron carbide in $CB–FeF_2$ could be explained by its smaller particle size. Due to the smaller particle size, the reaction between iron nanoparticles and FCB is fast, and the formation of iron carbide is mitigated. The smaller the particle size of the fluorinated carbon, the faster is the reaction with iron nanoparticles and hence no formation of iron carbide is observed in the case of FCB. However, the iron carbide content is large in the case of $G–FeF_2$ compared to $PC–FeF_2$ (the opposite is expected because of the small particle size of FG compared to FPC); this could be due to the availability of free carbon in the precursor (F/C ratio 0.95) which could readily react with iron nanoparticles and form iron carbide.

To investigate the microstructure of the nanocomposites, scanning electron microscopy (SEM) and transmission electron microscopy (TEM) analysis was performed on these nanocomposites. Fig. 3 shows the SEM images of the nanocomposites. Additional low magnification SEM images were shown in Fig. S3 (see ESI†). The bulk morphologies were similar to unreacted precursors. In the case of $PC–FeF_2$ (Fig. 3a), FeF_2 crystallites are embedded in carbon layers. No FeF_2 particles are seen on the surface of the sample. However, in the case of $CB–FeF_2$ (Fig. 3b), some of the FeF_2 crystallites are protruding on the surface, and few crystallites (up to 50 nm) are also seen on the surface (shown with arrows). This could be due to the high surface to volume ratio of the sample. The $G–FeF_2$ (Fig. 3c) looks similar to $PC–FeF_2$, and no FeF_2 particles are seen on the surface. All the particles are embedded in the carbon layers. The $CF–FeF_2$ (Fig. 3d) sample appears quite different from all the nanocomposites. Apart from the FeF_2 crystallites embedded in the carbon layers, a large number of FeF_2 crystallites (up to 300 nm) can be observed on the surface of the fibers. The reason for such behavior is not understood at present.

Fig. 4 shows the bright-field TEM images of the $C–FeF_2$ nanocomposites. All the nanocomposites show a similar morphology. The high resolution TEM image of $G–FeF_2$ is shown in Fig. S4 (see ESI†). The FeF_2 crystallites are embedded in the carbon matrix. The crystallite sizes are in the range of 5–12 nm. Fig. 5 shows the SEAD patterns corresponding to the TEM images shown in Fig. 4. SAED of $PC–FeF_2$ (Fig. 5a), $CB–FeF_2$ (Fig. 5b) and $CF–FeF_2$ (Fig. 5d) exhibit a similar pattern and demonstrate the nanocrystalline nature of the FeF_2. However, the SAED pattern of $CF–FeF_2$ shows additional rings in agreement with the lattice distances seen in iron carbide. In the case of $G–FeF_2$ (Fig. 5c) in addition to the nanocrystalline FeF_2 few rings with bright spots were observed, which is attributed to the graphite as the d-values of the spots match with the d-values from graphite.

Electron energy loss spectroscopy (EELS) was performed to further understand the electronic structure of carbon and valence state of iron fluoride. Carbon K-edge spectra are shown
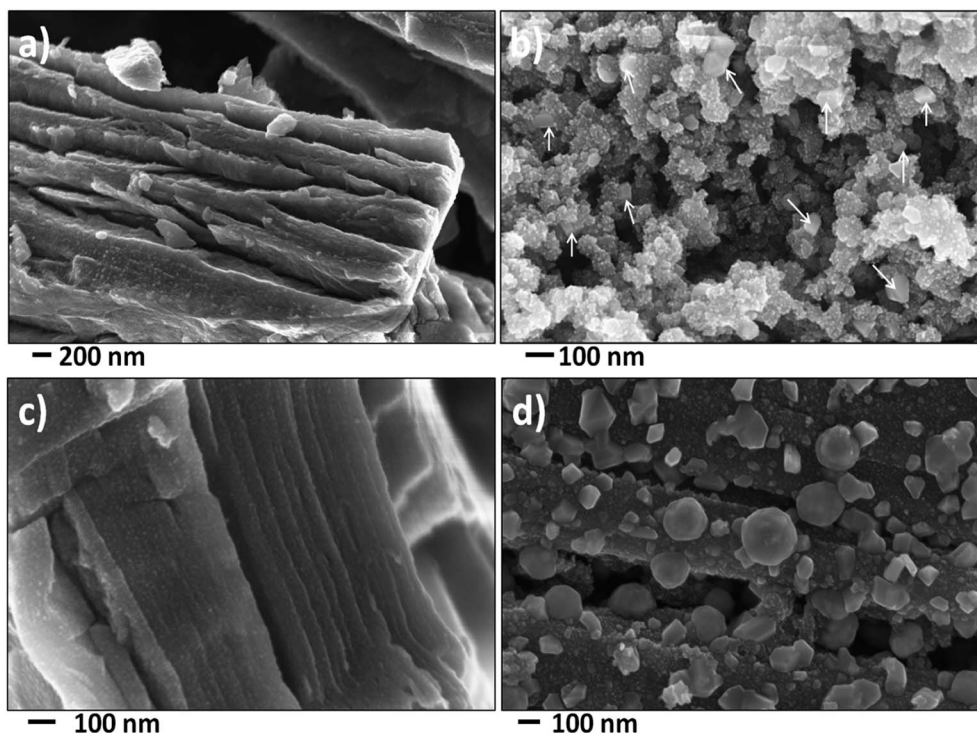

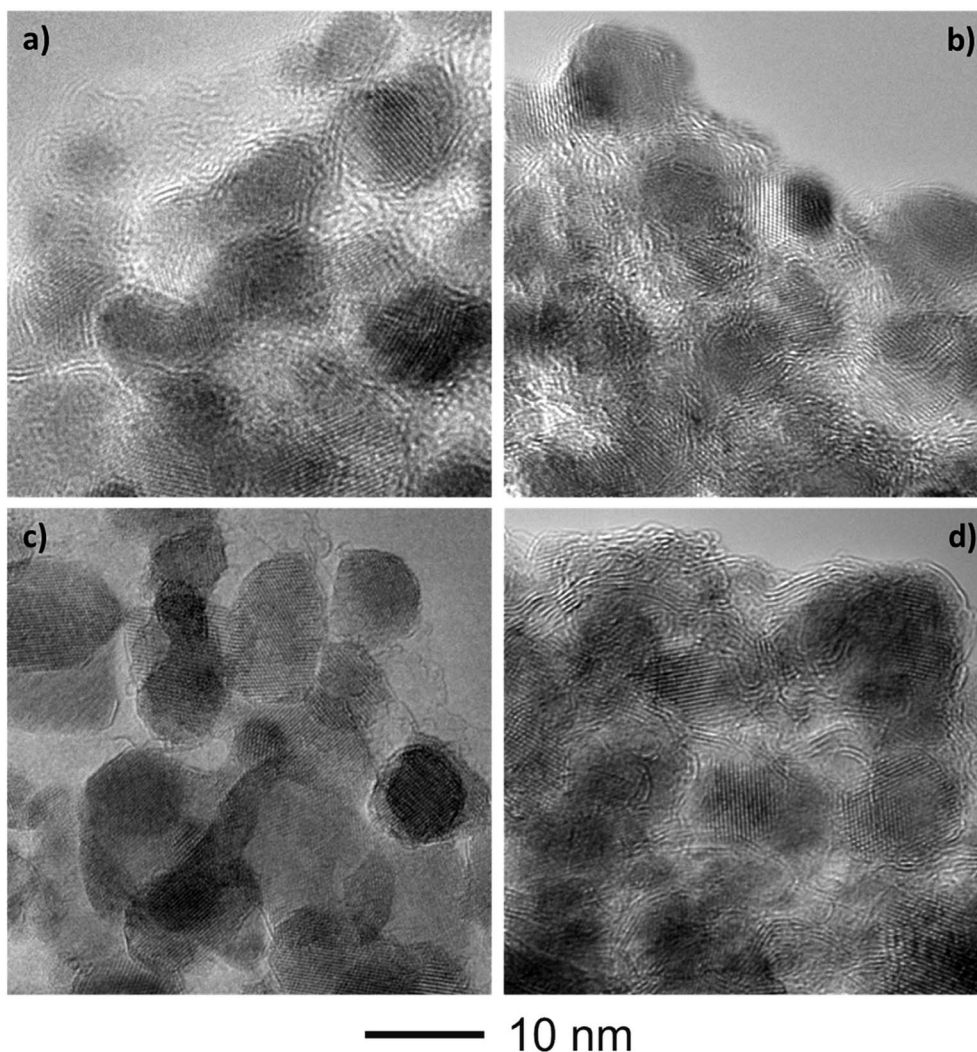Fig. 3 High resolution SEM images of (a) $PC–FeF_2$ (b) $CB–FeF_2$ (c) $G–FeF_2$ and (d) $CF–FeF_2$.

Fig. 4 Bright-field TEM images of (a) PC−FeF$_2$ (b) CB−FeF$_2$ (c) G−FeF$_2$ and (d) CF−FeF$_2$.

in Fig. 6a and the F-K edge and Fe-L edge is shown in Fig. 6b. The carbon spectra of all the nanocomposites show a typical shape for graphitic or amorphous carbon where the "Energy loss near edge structure" (ELNES) indicates two peaks for the transition of the C K-shell electrons to π*- (284.5 eV) and σ*- (290.5 eV) antibonding states.[31] The ELNES structure of G−FeF$_2$ shows the most defined peaks, which indicates a more ordered sp^2 hybridized carbon compared to the other three samples, where the structure is characteristic for amorphous carbon.[32] The F-K edge, the Fe-L$_3$ edge, and the Fe-L$_2$ edge are shown in Fig. 6b. In case of significant amounts of FeF$_3$, a pre-peak would be expected in EELS and XAS measurements at 684.6 eV.[31,33] The absence of this pre-peak in the EELS spectra rules out the presence of significant amounts of FeF$_3$. This suggests that the observation of Fe^{3+} in the Mössbauer spectra is due to oxidation of the sample.

The electrical resistivity of the samples was measured to understand the conducting nature of the composites. Fig. 7 shows the resistivities of C−FeF$_2$ nanocomposites. The resistivities of PC−FeF$_2$, CB−FeF$_2$, G−FeF$_2$ and CF−FeF$_2$ are 66, 1750, 7

and 314 ohm cm respectively. CB−FeF$_2$ composites showed high resistivity compared to PC−FeF$_2$, G−FeF$_2$ and CF−FeF$_2$. The large difference in the resistivity of CB−FeF$_2$ and other composites could be due to the lack of iron carbide in CB−FeF$_2$. Iron carbide shows semiconductivity or metallic conductivity depending on the composition.[34] Therefore the presence of iron carbide in PC−FeF$_2$, G−FeF$_2$ and CF−FeF$_2$ might result in the reduced resistivity. The very low resistivity of G−FeF$_2$ could be due to the large graphitic domains and the high carbon content.

Electrochemical studies

Even though the resistivity of CB−FeF$_2$ is high, initial electrochemical studies were performed without the addition of extra carbon as we aimed to understand the nature of the carbon precursor on the electrochemical properties of the nanocomposites. Fig. 8 shows the discharge/charge curves of C−FeF$_2$ nanocomposites for the first 20 cycles obtained at 25 °C. Capacities are calculated based on the total weight of the nanocomposite in the electrode (i.e., 90% of the total electrode weight). The total first discharge capacities of PC−FeF$_2$, CB−
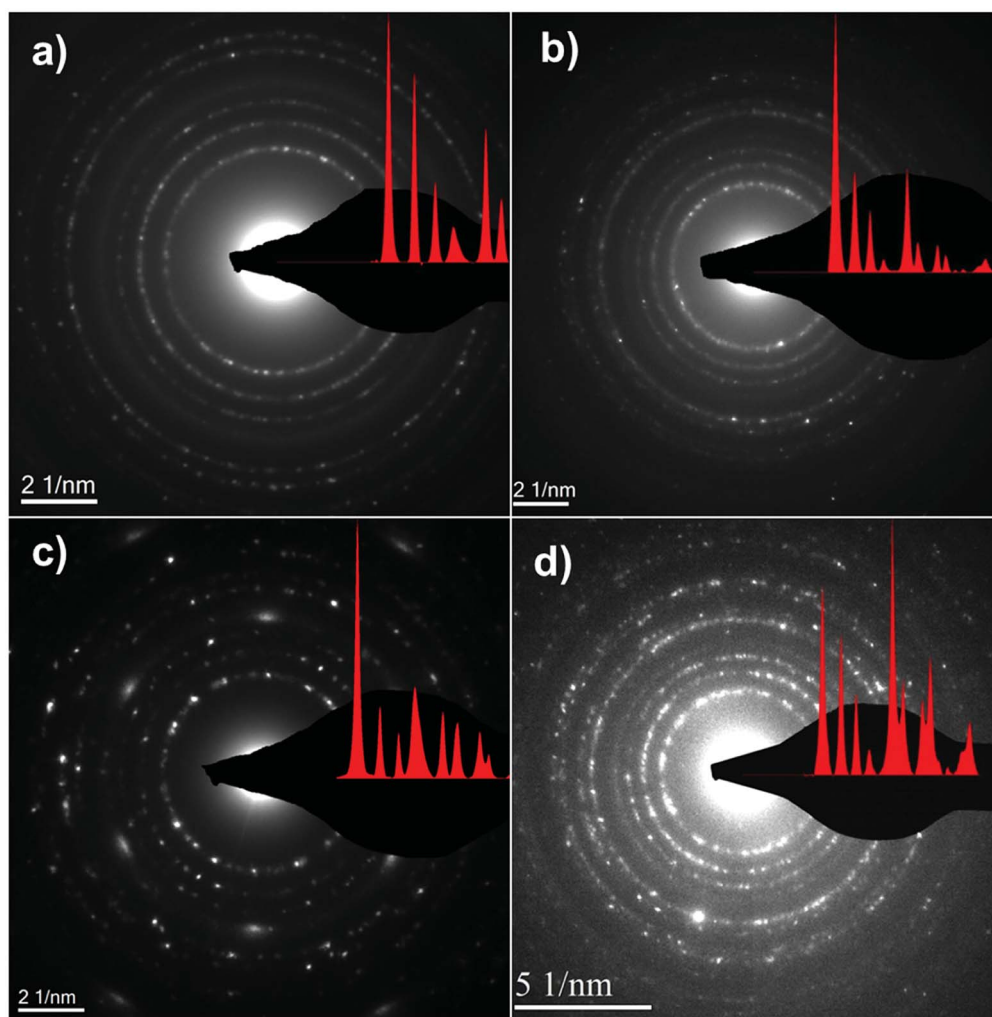
Fig. 5 Selective area electron diffraction (SAED) of TEM images shown in (a) $PC-FeF_2$ (b) $CB-FeF_2$ (c) $G-FeF_2$ and (d) $CF-FeF_2$.

FeF_2, $G-FeF_2$ and $CF-FeF_2$ are 326, 540, 442, and 225 mA h g^{-1} respectively. $C-FeF_2$ nanocomposites derived from FPC and FCF delivered much less capacity compared to the $CB-FeF_2$ and $G-FeF_2$ nanocomposites. The first discharge capacities correlated well with the particle size of the CFx precursors. Larger particle size resulted in less discharge capacity. It appears that, in the case of large particles, accessing the FeF_2 nanocrystallites embedded in the core of the particle is difficult. Consequently, some of the FeF_2 crystallites do not participate in the electrochemical reaction with lithium and hence less discharge capacity was observed. The first discharge curve of $C-FeF_2$ composite shows two voltage regions; sloping region between 3.0–1.8 V and by a plateau region between 1.8–1.3 V. Further, there is an additional voltage plateau observed in the case of $CF-FeF_2$, which could be due to inhomogeneity in particle size (evident from SEM, Fig. 3d). FeF_2 should react at a single voltage plateau with lithium.[35] Bigger particles of FeF_2 react at a lower voltage compared to nanocrystalline FeF_2 due to the sluggish kinetics, which might have resulted in two different voltage plateaus observed in $CF-FeF_2$. Indeed, two different sized FeF_2 crystallites were observed in $CF-FeF_2$ nanocomposites (Fig. 3d).

In addition to the plateau at $\sim$1.8 V, all the $C-FeF_2$ nanocomposites delivered significant capacity in the 3.0–1.8 V region. The discharge capacity contribution in the 3.0 V to 1.8 V region is 37 mA h g^{-1}, 42 mA h g^{-1}, 75 mA h g^{-1}, 54 mA h g^{-1} for $PC-FeF_2$, $CB-FeF_2$, $G-FeF_2$ and $CF-FeF_2$ respectively. This could be connected to the insertion of lithium into nanocrystalline FeF_2. Yamakawa *et al.* investigated the lithium insertion mechanism into nanocrystalline FeF_3 and FeF_2 by using solid-state NMR, XRD, and PDF analysis.[36] In the case of nanocrystalline FeF_2, they also observed significant capacity contribution in the 3.0 V to 1.8 V region, which was attributed to the insertion of Li in FeF_2. We can, therefore, attribute the capacity observed in the in the 3.0 V to 1.8 V region to the insertion of lithium into nanocrystalline FeF_2.

We also investigated the electrochemical performance of $C-FeF_2$ nanocomposites at 40 °C. Fig. 9 shows the discharge/charge curves of $C-FeF_2$ composites obtained at 40 °C. The first discharge capacities of $PC-FeF_2$, $CB-FeF_2$, $G-FeF_2$ and $CF-FeF_2$ are 390, 626, 507, and 318 mA h g^{-1} respectively. The discharge capacity increased with increase in temperature in all the cases. Similarly, the capacities, in the 3.0 V to 1.8 V region
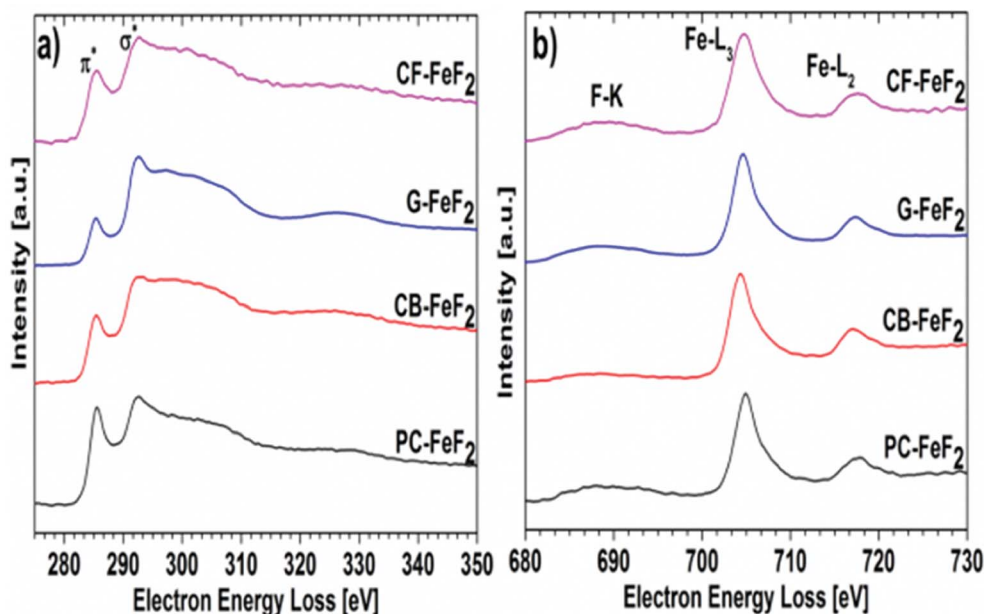
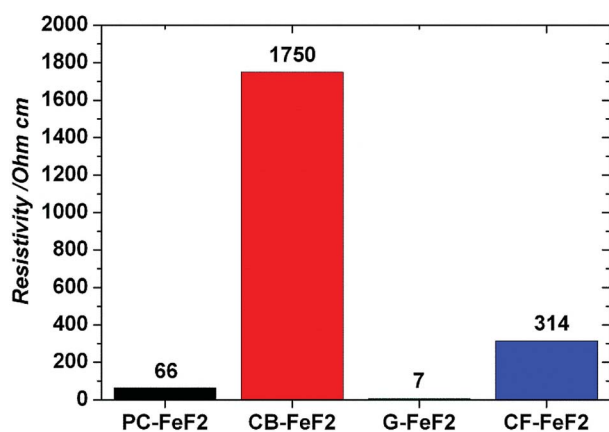**Fig. 6** Electron energy loss spectra (EELS) recorded for (a) carbon edge and (b) fluorine and iron edge.

Fig. 7 Resistivities of the C−FeF$_2$ nanocomposites.

also increased with an increase in cycling temperature. Fig. 10 shows the cycling behavior of C–FeF$_2$ nanocomposites obtained at 25 °C and 40 °C. The electrochemical performance of CB–FeF$_2$ and G–FeF$_2$ correlated well with the particle size and values of electrical resistivity. In the case of C–FeF$_2$ derived from FPC and FCF, capacity faded rapidly and the reversible capacity reduced to 20 mA h g^{-1} within a few cycles. CB–FeF$_2$ shows high initial capacity, but capacity faded continuously with cycling. A reversible capacity of 145 mA h g^{-1} was obtained after 70 cycles at 25 °C. In contrast, G–FeF$_2$ composites showed less reversible capacity and rapid capacity fading initially compared to CB–FeF$_2$, but the capacity stabilized after a few cycles. A reversible capacity of 163 mA h g^{-1} was obtained after 100 cycles at 25 °C. At 40 °C, CB–FeF$_2$ samples showed much faster capacity fading, a reversible capacity of 184 mA h g^{-1} was obtained after 30 cycles. On the other hand, in G–FeF$_2$ nanocomposites shows

less capacity fading and high reversible capacity, a reversible capacity of 340 mA h g^{-1} was obtained after 30 cycles, which is almost two times to that of CB–FeF$_2$ nanocomposites. The smaller particle size of FCB resulted in high initial capacity due to the reaction of all FeF$_2$ particles but resulted in continuous capacity fading as the carbon in which the FeF$_2$ nanocrystallites embedded is resistive. In contrast, in G–FeF$_2$, capacity faded initially, probably due to the larger particle size of CFx but showed much better cycling stability due to the high conducting nature of graphitic carbon backbone. Pereira *et al.* investigated the electrochemical properties of C–FeF$_2$ nanocomposites (at 60 °C) synthesized by a combination of chemical and mechanical milling.[9] The C–FeF$_2$ nanocomposites showed high capacity of 420 mA h g^{-1} in the first cycle, but capacity faded rapidly with cycling, similar to CB–FeF$_2$ nanocomposites investigated here.

CB–FeF$_2$ composites delivered high reversible capacity, but capacity faded rapidly with cycling due to the low electronic conductivity of the carbon backbone. Enhancing the electronic conductivity CB–FeF$_2$ might mitigate the capacity fading. Therefore, we deliberately added carbon nanofibers (CNF) to CB–FeF$_2$ nanocomposite and electrode were made similar to CNF free CB–FeF$_2$ electrodes. Fig. S5† shows the EIS spectra of PC–FeF$_2$, CB–FeF$_2$, G–FeF$_2$, CF–FeF$_2$ and PC–FeF$_2$ + CNF cells. The resistance of the cells decreased in the order of CB–FeF$_2$ > CF–FeF$_2$ > PC–FeF$_2$ > G–FeF$_2$ which is consistent with DC electronic conductivity measurements. After mixing of CNF, CB–FeF$_2$ cells showed lower resistance compared to all other C–FeF$_2$ cells, which confirms that the overall resistance of the CB–FeF$_2$ electrode reduced significantly after the addition of CNF. Fig. 11 shows the electrochemical performance of CB–FeF$_2$ + CNF cells cycled at 25 °C and 40 °C. The cyclic performance of the cells was similar to the cells of CNF free CB–FeF$_2$ cells. These results elucidate that the electronic conductivity of the carbon which is
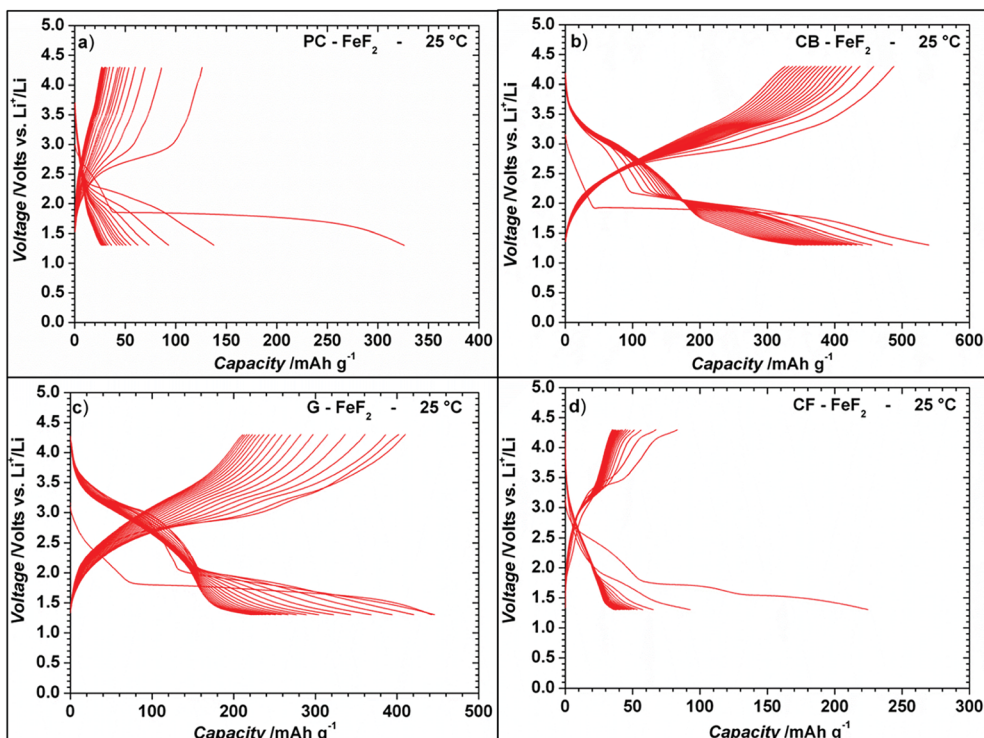
Fig. 8 Electrochemical discharge/charge curves of C−FeF$_2$ nanocomposites for the first 20 cycles at 25 °C. The discharge and charge curves are obtained at a constant current of 20 mA g^{-1} in the voltage window 1.3−4.3 V. The capacities are calculated with respect to total weight of the nanocomposite (*i.e.*, 90% of the total electrode weight).
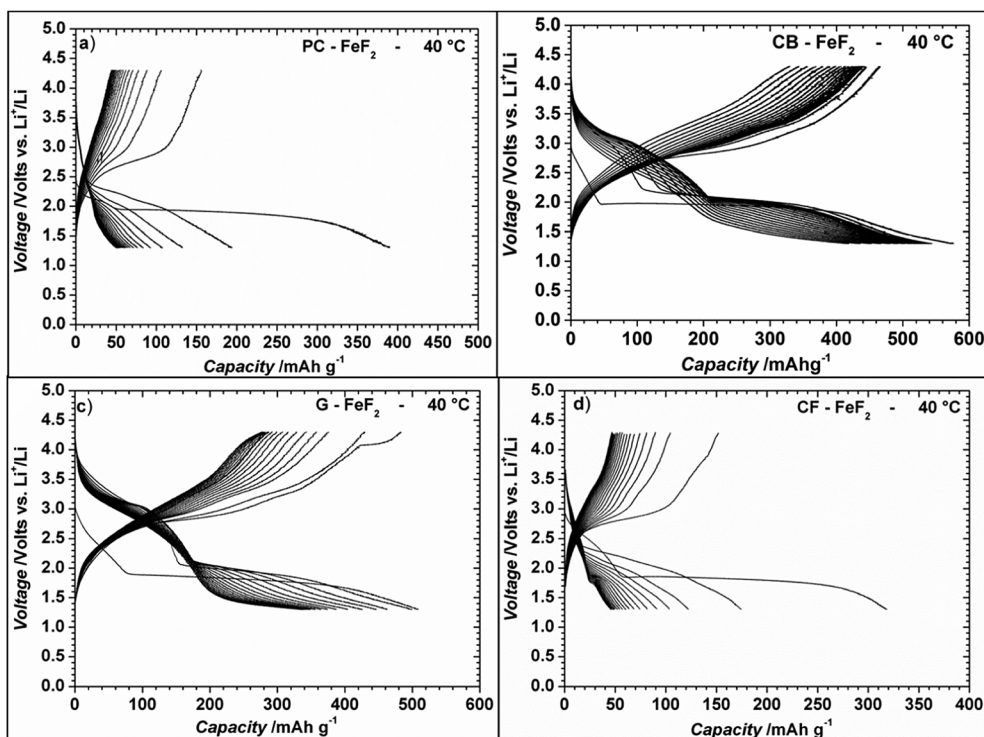

Fig. 9 Electrochemical discharge/charge curves of C−FeF$_2$ nanocomposites for the first 20 cycles at 40 °C. The discharge and charge curves were obtained at a constant current rate of the 20 mA g^{-1} in the voltage window 1.3−4.3 V. The capacities are calculated with respect to total weight of the nanocomposite (*i.e.*, 90% of the total electrode weight).
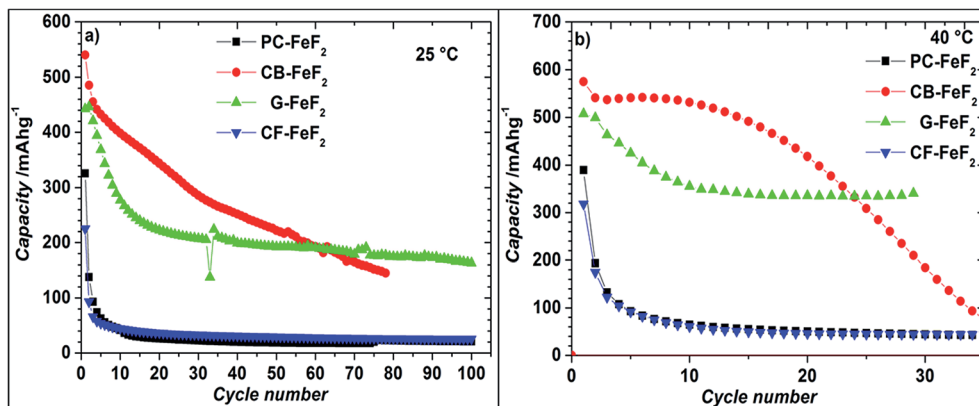
Fig. 10 Electrochemical cycling of C–FeF$_2$ at a constant current of 20 mA g^{-1} in the voltage window of 1.3–4.3 V (a) at 25 °C and (b) at 40 °C. The capacities are calculated with respect to the total weight of the nanocomposite (*i.e.*, 90% of the total electrode weight).

Fig. 11 Electrochemical cycling of CB–FeF$_2$ + CNF at a constant current of 20 mA g^{-1} in the voltage window of 1.3–4.3 V (a) at 25 °C and (b) at 40 °C. The capacities are calculated with respect to total weight of the nanocomposite (*i.e.*, 80% of the total electrode weight).
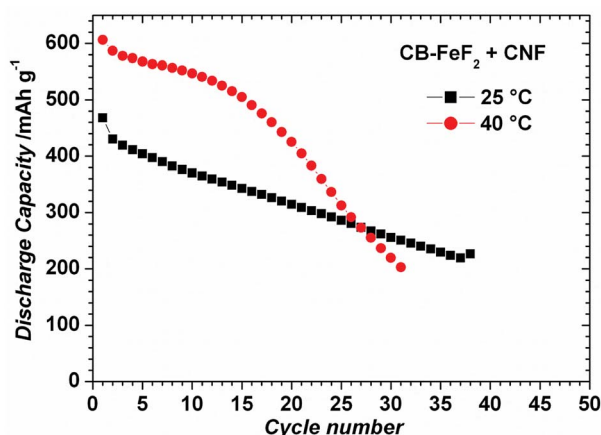
in direct contact with FeF$_2$ nanocrystallites plays a major role in determining the electrochemical performance of FeF$_2$ while the total amount of even highly conductive carbon that is present in the electrode plays an inferior role.

Conclusion

Four different C–FeF$_2$ nanocomposites were synthesized by reacting Fe(CO)$_5$ with four different CFx precursors at 250 °C. The four C–FeF$_2$ nanocomposites differed in the initial particle size of the carbon matrix, and electronic conductivity of the resulting C–FeF$_2$ nanocomposites. Both particle size and the electronic conductivity play a crucial role in determining the electrochemical performance of the C–FeF$_2$ nanocomposites. G–FeF$_2$ nanocomposites show less capacity fading and highly reversible capacity at 40 °C. Here, a reversible capacity of 340 mA h g^{-1} was obtained after 30 cycles. The reversible capacity of G–FeF$_2$ nanocomposites can be improved further by reduction of the initial particle size. Further, the electronic conductivity of the carbon that is directly attached to the FeF$_2$

nanocrystallites plays a major role in determining the electrochemical performance of FeF$_2$ rather than the total amount of the carbon that is present in the electrode. The results obtained here provide an opportunity to study and understand the requirements for the design of conversion electrode materials for reversible lithium storage.

Conflicts of interest

There are no conflicts to declare.

Acknowledgements

References

1 D. Andre, S. J. Kim, P. Lamp, S. F. Lux, F. Maglia, O. Paschosa and B. Stiaszny, *J. Mater. Chem. A*, 2015, **3**, 6709–6732.

2 C. Li, K. Chen, X. Zhou and J. Maier, *NPJ Comp. Mat.*, 2018, **4**, 22.

3 H. Li, P. Balaya and J. Maier, *J. Electrochem. Soc.*, 2004, **151**, A1878–A1885.

4 G. G. Amatucci and N. Pereira, *J. Fluorine Chem.*, 2007, **128**, 243–262.

5 J. Cabana, L. Monconduit, D. Larcher and M. R. Palacin, *Adv. Mater.*, 2010, **22**, E170–E192.

6 M. Fichtner, *Phys. Chem. Chem. Phys.*, 2011, **13**, 21186–21195.

7 F. Badway, N. Pereira, F. Cosandey and G. G. Amatucci, *J. Electrochem. Soc.*, 2003, **150**, A1209–A1218.

8 I. Plitz, F. Badway, J. Al-Sharab, A. DuPasquier, F. Cosandey and G. G. Amatucci, *J. Electrochem. Soc.*, 2005, **152**, A307–A315.

9 N. Pereira, F. Badway, M. Wartelsky, S. Gunn and G. G. Amatucci, *J. Electrochem. Soc.*, 2009, **156**, A407–A416.

10 T. Li, L. Li, Y. L. Cao, X. P. Ai and H. X. Yang, *J. Phys. Chem. C*, 2010, **114**, 3190–3195.

11 L. Li, F. Meng and S. Jin, *Nano Lett.*, 2012, **12**, 6030–6037.

12 S. W. Kim, D. H. Seo, H. Gwon, J. Kim and K. Kang, *Adv. Mater.*, 2010, **22**, 5260–5264.

13 C. Li, L. Gu, S. Tsukimoto, P. A. van Aken and J. Maier, *Adv. Mater.*, 2010, **22**, 3650–3654.

14 C. Li, L. Gu, J. Tong, T. Susumu and J. Maier, *Adv. Funct. Mater.*, 2011, **21**, 1391–1397.

15 C. Li, L. Gu, J. Tong and J. Maier, *ACS Nano*, 2011, **5**, 2930–2938.

16 B. Li, D. W. Rooney, N. Zhang and K. Sun, *ACS Appl. Mater. Interfaces*, 2013, **5**, 5057–5063.

17 Y. Ma, C. Zhang, G. Jia and J. Y. Lee, *J. Mater. Chem.*, 2012, **22**, 7845–7850.

18 K. Rui, Z. Wen, Y. Lu, J. Jin and C. Shen, *Adv. Energy Mater.*, 2015, **5**, 1401716.

19 Y. Lu, Z. Wen, J. Jin, X. Wu and K. Rui, *Chem. Commun.*, 2014, **50**, 6487–6490.

20 Y. Lu, Z. Wen, J. Jin, K. Rui and X. Wu, *Phys. Chem. Chem. Phys.*, 2014, **16**, 8556–8562.

21 Y. Lu, Z. Wen, K. Rui, X. Wu and Y. Cui, *J. Power Sources*, 2013, **244**, 306–311.

22 R. Prakash, A. K. Mishra, A. Roth, Ch. Kübel, T. Scherer, M. Ghafari, H. Hahn and M. Fichtner, *J. Mater. Chem.*, 2010, **20**, 1871–1876.

23 R. Prakash, C. Wall, A. K. Mishra, C. Kübel, M. Ghafari, H. Hahn and M. Fichtner, *J. Power Sources*, 2011, **196**, 5936–5944.

24 C. Wall, R. Prakash, C. Kübel, H. Hahn and M. Fichtner, *J. Alloys Compd.*, 2012, **530**, 121–126.

25 M. Anji Reddy, B. Breitung, V. S. K. Chakravadhanula, C. Wall, M. Engel, C. Kübel, A. K. Powell, H. Hahn and M. Fichtner, *Adv. Energy Mater.*, 2013, **3**, 308–313.

26 B. Breitung, M. Anji Reddy, V. S. K. Chakravadhanula, M. Engel, C. Kübel, A. K. Powell, H. Hahn and M. Fichtner, *Beilstein J. Nanotechnol.*, 2013, **4**, 705–713.

27 M. Anji Reddy, B. Breitung, C. Wall, S. Trivedi, V. S. K. Chakravadhanula, M. Helen and M. Fichtner, *Energy Technol.*, 2016, **4**, 201–211.

28 L. Lutterotti and P. Scardi, *J. Appl. Crystallogr.*, 1990, **23**, 246–252.

29 S. Ramasamy, J. Jiang, H. Gleiter, R. Birringer and U. Gonser, *Solid State Commun.*, 1990, **74**, 851–855.

30 G. LeCaer and E. Bauer-Grosse, *Hyperfine Interact.*, 1989, **47**, 55–67.

31 A. A. El-Barbary, S. Trasobares, C. P. Ewels, O. Stephan, A. V. Okotrub, L. G. Bulusheva, C. J. Fall and M. I. Heggie, *J. Phys.: Conf. Ser.*, 2006, **26**, 149–152.

32 K. N. Kushita and K. Hojou, *Ultramicroscopy*, 1991, **35**, 289–293.

33 F. Cosandey, J. F. Al-Sharab, F. Badway, G. G. Amatucci and P. Stadelmann, *Microsc. Microanal.*, 2007, **13**, 87–95.

34 M.-C. Lee and G. Simkovich, *Metal. Trans. A*, 1987, **18**, 485.

35 F. Wang, H.-C. Yu, M.-H. Chen, L. Wu, N. Pereira, K. Thornton, A. Van der Ven, Y. Zhu, G. G. Amatucci and J. Graetz, *Nat. Commun.*, 2012, **3**, 1201.

36 N. Yamakawa, M. Jiang, B. Key and C. P. Grey, *J. Am. Chem. Soc.*, 2009, **131**, 10525–10536.